AIP | Review of Scientific Instruments

Pattern-integrated interference lithography instrumentation

G. M. Burrow, M. C. R. Leibovici, J. W. Kummer, and T. K. Gaylord

Citation: Rev. Sci. Instrum. **83**, 063707 (2012); doi: 10.1063/1.4729666
View online: http://dx.doi.org/10.1063/1.4729666
View Table of Contents: http://rsi.aip.org/resource/1/RSINAK/v83/i6
Published by the American Institute of Physics.

Pattern-integrated interference lithography instrumentation

G. M. Burrow, M. C. R. Leibovici, J. W. Kummer, and T. K. Gaylord
School of Electrical and Computer Engineering, Georgia Institute of Technology, Atlanta, Georgia 30332-0250, USA

(Received 10 May 2012; accepted 2 June 2012; published online 21 June 2012)

Multi-beam interference (MBI) provides the ability to form a wide range of sub-micron periodic optical-intensity distributions with applications to a variety of areas, including photonic crystals (PCs), nanoelectronics, biomedical structures, optical trapping, metamaterials, and numerous subwavelength structures. Recently, pattern-integrated interference lithography (PIIL) was presented as a new lithographic method that integrates superposed pattern imaging with interference lithography in a single-exposure step. In the present work, the basic design and systematic implementation of a pattern-integrated interference exposure system (PIIES) is presented to realize PIIL by incorporating a projection imaging capability in a novel three-beam interference configuration. A fundamental optimization methodology is presented to model the system and predict MBI-patterning performance. To demonstrate the PIIL method, a prototype PIIES experimental configuration is presented, including detailed alignment techniques and experimental procedures. Examples of well-defined PC structures, fabricated with a PIIES prototype, are presented to demonstrate the potential of PIIL for fabricating dense integrated optical circuits, as well as numerous other subwavelength structures. © *2012 American Institute of Physics*. [http://dx.doi.org/10.1063/1.4729666]

I. INTRODUCTION

Multi-beam interference (MBI) provides the ability to form a wide variety of sub-micron periodic optical-intensity distributions in one, two, and three dimensions. Accordingly, MBI has been used in a wide variety of application areas including nanoelectronics,[1,2] photonic crystals (PCs),[3–5] biomedical structures,[6–8] optical trapping,[9–11] metamaterials,[12,13] and numerous subwavelength structures.[14–18] As a result of the broad application of the MBI, research has demonstrated numerous periodic and quasi-periodic patterns with specific space-group symmetries by careful selection of individual beam amplitudes, polarizations, and wavevector configurations.[19–22] These same parameters are also used to optimize the contrast of the resulting interference lattice, providing lithographically useful patterning possibilities.[23–26] As such, several optical configurations and lithographic techniques have been developed to incorporate interference lithography (IL), providing the potential for simple, rapid, wafer-scale, and low-cost fabrication.

Recently, pattern-integrated interference lithography (PIIL) was presented that integrates superposed pattern imaging with IL.[27–29] The result is a complex optical-intensity distribution composed of an MBI-defined periodic lattice modified by an integrated mask pattern image to form functional elements. To implement PIIL, a pattern-integrated interference exposure system (PIIES) was introduced that incorporates a projection imaging capability in a novel three-beam interference configuration in order to fabricate, in a single-exposure step, a two-dimensional periodic PC lattice with non-periodic functional elements integrated into the periodic pattern. In the present work, the basic design of the experimental system is presented. A fundamental ZEMAX (Ref. 30) optimization methodology is used to model the system and predict MBI-patterning performance. Next, the prototype PIIES experimental configuration is presented, including detailed alignment techniques and experimental procedures, serving as a foundation for future system design and enhancements. Examples of well-defined PC structures, fabricated with a PIIES prototype, are presented to demonstrate the potential of PIIL for fabricating dense integrated optical circuits, as well as numerous other subwavelength structures.

II. THREE-BEAM PATTERN-INTEGRATED INTERFERENCE EXPOSURE SYSTEM

A conceptual three-beam PIIES configuration is depicted in Fig. 1(a).[27–29] To ensure a high-contrast interference pattern for a wide range of periodic-lattice symmetries, a combination of half-wave plates and beam-splitter cubes was used to control individual-beam linear polarizations and amplitudes as reported previously by our group.[31] To demonstrate the functionality of the system, the PIIES configuration presented here is arranged to produce a square-lattice interference pattern by implementing the wavevector configuration of Fig. 1(b). Initially, the multiple beams propagate parallel to the optical axis of the system at a common beam displacement, d_{beam}. To achieve the desired interference patterning capability, the multiple optical components are positioned such that each interfering beam is collimated at the exit of the final objective lens, intersecting at the sample plane at a specific common incidence angle, θ_S. The result is a uniform-periodic interference pattern with a lattice constant, a_{sq}, given by

$$a_{\text{sq}} = \lambda/(\sqrt{2}\sin\theta_S), \tag{1}$$

where λ is the source freespace wavelength. If the three interfering beams are adjusted such that their projections on the sample plane are separated equally by 120°, while

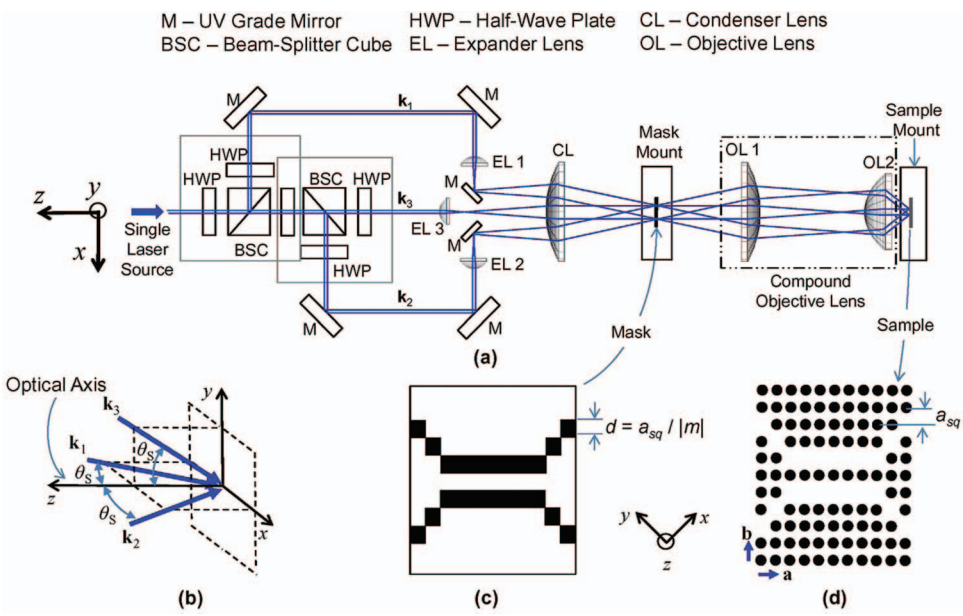

FIG. 1. Three-beam pattern-integrated interference exposure system (PIIES).[28] (a) A ray trace depicts the propagation of $\mathbf{k}_1$, $\mathbf{k}_2$, and $\mathbf{k}_3$ through the PIIES optical configuration, implementing (b) a wavevector configuration required to produce a square-lattice interference pattern with collimated beams at the sample plane. (c) A functional-element amplitude mask is placed at the mask plane with features sizes of $d = a_{sq}/|m|$, where m is the magnification due to the compound objective lens. (d) The result is an optical-intensity distribution of an integrated non-periodic functional element in an all-surrounding, high-spatial-frequency periodic square lattice, enabling single-exposure fabrication of a functional device, such as a PC waveguide coupler.[32]

maintaining a common θ_S, a hexagonal periodic lattice is formed with a lattice constant of

$$a_{\text{hex}} = 2\lambda/(3\sin\theta_S)\,. \tag{2}$$

The multiple beams, expander lenses, and condenser lens (CL) also serve as the illumination system for the integrated image projection capability. In the present PIIES configuration, a mask plane is collocated at the condenser lens back focal plane where the three expanded beams intersect, providing coherent multi-beam off-axis illumination of an object such as the amplitude mask depicted in Fig. 1(c). The purpose of this mask is two-fold. First, the transparent areas of the mask allow the multiple beams to pass through and form the desired interference pattern at the sample plane. Second, the opaque areas of the mask block and diffract the illuminating beams, portions of which are collected by the objective lens and focused at the sample plane. These projected mask elements effectively block the multiple interfering beams at the sample plane, thereby preventing or altering the formation of portions of the interference pattern at areas corresponding to the functional elements defined by the mask features with dimensions, $d = a_{\text{sq}}/|m|$, where m is the magnification due to the compound objective lens. The result is an optical-intensity distribution containing integrated non-periodic functional elements in an all-surrounding, high-spatial-frequency MBI-defined periodic pattern. This distribution may, in turn, be recorded in a photoresist, in a single-exposure step, to form functional devices, such as the PC waveguide coupler depicted in Fig. 1(d).[32]

A. System design

The basic design of the PIIES configuration begins with a novel lens-based system to implement three-beam interference. To ensure an interference pattern with uniform periodicity and sufficient area, the interfering beams should be collimated as depicted by the ray trace of $\mathbf{k}_1$ and $\mathbf{k}_2$ ($\mathbf{k}_3$ is not shown for clarity) in Fig. 2. Here it is seen that collimated beams are produced when the individual beams are focused at the front focal plane of the final objective lens. In general, larger beam displacements, d_{beam}, and shorter focal lengths for the second objective lens, f_{OL2}, result in larger incidence angles at the sample plane, corresponding to smaller lattice constants. This relationship suggests that an objective lens system with a large numerical aperture is desired for the PIIES configuration.

To obtain a large numerical aperture, thereby increasing the range of possible lattice constants and improving the projected image resolution, a two-lens configuration was selected for the compound objective lens system depicted in Fig. 2. This allows the power of the objective lens system to be divided between two lenses, thereby increasing the maximum possible θ_S, while reducing lens aberrations for the integrated projection imaging capability. Of course, modern projection objective lens designs often include numerous low-power lens elements to minimize aberrations including spherical, coma, astigmatism, field curvature, and distortion.[33] In the rudimentary design presented here, only on-axis aberrations were considered. Accordingly, aspheric lens were selected for the two objective lenses to reduce on-axis spherical aberration. Similarly, an aspheric lens was also selected for the condenser lens to minimize distortions to the collimated interfering beams.

Aspheric lenses are designed to provide a common focal plane for axial rays, regardless of their radial position, thereby reducing off-axis aberrations. To take advantage of this fact, the compound objective lens design included the requirement

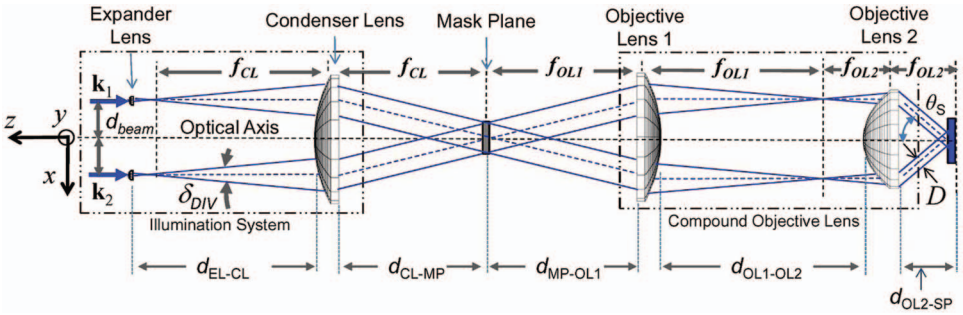

FIG. 2. PIIES configuration. The prototype system is arranged as a 6*f* configuration using large-diameter aspheric lenses. Expander lenses are added to ensure that the multiple beams are focused at the front focal plane of objective lens 1, providing collimated interfering beams at the sample plane and coherent illumination of a mask located at the mask plane. The incidence angle at the sample plane, θ_S, may be increased or decreased by adjusting the radial distance of the individual beams, d_{beam}, from the optical axis.

that the beams propagate parallel to the optical axis upon exiting the first objective lens and at the entrance to the second objective lens as depicted in Fig. 2. Similarly, the design required that the beams incident on the condenser lens also be parallel to the optical axis. To satisfy these two conditions, the condenser lens and first objective lens are separated by the sum of the focal lengths, f_{CL} and f_{OL1}, of the two lenses. As a result, a general relationship between the beam displacement and resulting incidence angle at the sample plane is given by

$$\theta_S \sim \tan^{-1}\left(d_{beam}/f_{OL2}\right). \tag{3}$$

To complete the basic PIIES design and integrate an image projection capability, the multiple beams must be conditioned such that they focus at the front focal plane of the second objective lens, while simultaneously illuminating a pattern mask located at the front focal plane of the first objective lens as depicted in Fig. 2. This is accomplished through the selection and placement of one or more expander lenses prior to the condenser lens. It should be noted that more complex systematic optical system designs may be considered to produce collimated interfering beams at the sample plane, while improving the system projection imaging capability. However, in the work presented here, a 6*f* configuration is chosen to satisfy the collimating requirements and provide a relatively simple low-cost prototype to demonstrate the PIIL method.

The resulting relationship between the diameter of the collimated beam, D, which determines the area of interference, and the beam divergence, δ_{DIV}, at the condenser lens is given by

$$D \propto \tan\left(\delta_{DIV}/2\right) \propto 1/f_{EL}, \tag{4}$$

where f_{EL} is the effective focal length of the expander lens system. The relationships given by Eqs. (3) and (4) both suggest that a large-diameter lens is preferred for both the condenser lens and the first objective lens. However, the focal length of these two lenses may be longer to reduce the power, and therefore the aberrations of the PIIES configuration. Accordingly, appropriate commercially available large-diameter broadband antireflection-coated aspheric lenses were used for the condenser and first objective lenses (ThorLabs, AL100200-B).[34] To increase the imaging numerical aperture of the compound objective lens system, a higher power lens with smaller focal length was selected for the second objective lens (ThorLabs, AL7560-A).

The resulting prototype PIIES configuration of Fig. 2 allows for a wide range of lattice constants and translational symmetries that vary from square to hexagonal, as determined by the radial displacement and arrangement of the three beams with respect to the optical axis. Based on the relationship given by Eq. (3) and the equations for the square and hexagonal lattice constants given by Eqs. (1) and (2), respectively, the lattice constant may be increased or decreased by adjusting the radial distance of the individual beams from the optical axis.

B. ZEMAX system optimization

To determine the positioning and alignment requirements for the various optical elements within the PIIES configuration, a ray-tracing simulation was performed using ZEMAX optical design software to model the beam propagation through the system.[35]

Using the lens specifications obtained from Thorlabs datasheets and the ZEMAX optimization algorithm described in the Appendix, the beam displacement, d_{beam}, and the inter-lens distances, $d_{\text{EL-CL}}$, $d_{\text{CL-MP}}$, $d_{\text{MP-OL1}}$, $d_{\text{OL1-OL2}}$, and $d_{\text{OL2-SP}}$, as depicted in Fig. 2, were set as variable parameters to optimize jointly the following: (1) collimation of the beam at the mask plane, (2) centering of the beam on the origin at the mask plane, (3) axial beam propagation between first and second objective lenses, (4) collimation of the beam at the sample plane, (5) centering of the beam on the origin at the sample plane, and (6) achieving the specified value of θ_S at the sample plane.

Physical constraints of the opto-mechanical system presented here limited beam displacement to a minimum value of approximately 5 mm from the optical axis. This value results in an approximate minimum incidence angle of $\theta_S \approx 5^\circ$. For θ_S larger than 30°, the beam becomes vignetted due to clear aperture limitations of the second objective lens. This limitation requires the beam diameter to be reduced for larger incidence angles corresponding to the beam displacement from the optical axis. This, in turn, reduces the beam diameter at the sample plane, D, resulting in a reduced area of

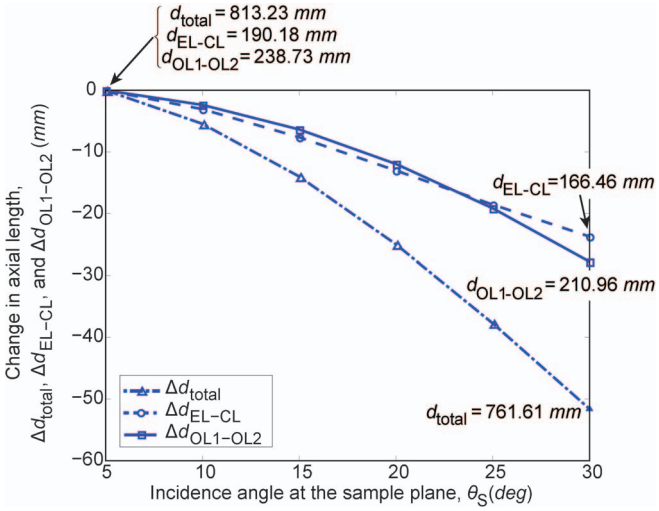

FIG. 3. The change in the axial lengths, $\Delta d_{EL\text{-}CL}$, $\Delta d_{OL1\text{-}OL2}$, and Δd_{total} are plotted as a function of the incidence angle, θ_S, at the sample plane.

interference. In the simulations presented here, the incidence angle at the sample plane ranges from $5 \leq \theta_S \leq 30°$.

Experimentally feasible values of d_{beam} and inter-lens distances were found that satisfy the above constraints. Of note, $d_{EL\text{-}CL}$, $d_{OL1\text{-}OL2}$, and the PIIES total length d_{total}, measured from the expander lens to the sample plane, were found to vary with θ_S. Figure 3 illustrates the change in axial length of $\Delta d_{EL\text{-}CL}$, $\Delta d_{OL1\text{-}OL2}$, and Δd_{total} as a function of θ_S. Here d_{total} decreases from 813.23 mm to 761.61 mm for θ_S ranging from 5° to 30°, resulting in a PIIES total length difference Δd_{total} of 251.61 mm for $\theta_S = 30°$.

These results suggest that the condenser lens, mask mount, and first objective lens may be fixed relative to one another, while the beam displacing optics, expander lenses, second objective lens, and sample mount require adjustment for each desired lattice constant and translational symmetry. Accordingly, appropriate translation stages are required to mount the optics and adjust the lens positions as θ_S is changed.

C. Predicted system performance

Using the ZEMAX optimization routine described in Sec. II B, the simulated PIIES performance was analyzed for the full range of beam incidence angles for both the square and hexagonal wavevector configurations. For θ_S varying from 5° to 30°, the lattice constant for square-lattice translation symmetry measured at the origin of the sample plane, a_{sq0}, ranges from 2.952 to 0.514 μm. For hexagonal-lattice translation symmetry, the lattice constant measured at the origin of the sample plane, a_{hex0}, ranges from 2.78 to 0.485 μm. However, the beam is slightly divergent at the sample plane, resulting in a small range of incidence angles for the rays. Thus, the beam produces a range of lattice constants, Δa_{sq} and Δa_{hex}, for both translational symmetries, ranging from 3.1% to 1.5%. In addition, the initial circular cross section of the beam is inevitably modified during its propagation through the PIIES and its projection on the sample plane decreases as θ_S increases. Thus, the circular overlap area of the three beams at the sample plane, A_{SP}, ranges from 60.82 to 19.63 mm^2, with an important drop of the overlap area as the incidence angle approaches $\theta_S = 30°$, where the beam starts to become vignetted by the second objective lens clear aperture. The resulting simulated d_{beam}, a_{sq0}, Δa_{sq}, a_{hex0}, Δa_{hex}, and A_{SP} values are presented in Table I.

The ZEMAX model confirms that the PIIES design is capable of generating incident angles at the sample plane ranging from $5 < \theta_S < 30°$. Furthermore, the PIIES is capable of producing photonic crystal structures varying between square and hexagonal translational symmetry, exhibiting submicron periodicity with good uniformity over a surface area of at least 35 mm^2 while the beams are not vignetted.

While the basic PIIES MBI patterning may be verified in ZEMAX as presented here, the system also includes an integrated imaging system and should be modeled as well. The version of ZEMAX used in the current work provides coherent image predictions by conducting a Fourier analysis of the complex system optical transfer function, accounting for the finite passband and other diffraction-related effects of the real optical system.[35] This method assumes a single extended coherent illumination source and approximates the coherent transfer function to form the predicted image. However, ZEMAX does not provide a means to model multi-beam off-axis mask illumination. Due to the unique design of the PIIES, ZEMAX, as well as other commercial image simulation softwares, are not able to simulate simultaneously the MBI-defined interference pattern with integrated functional elements resulting from the projected mask image. A new model to analyze the quality of the PIIES pattern-integrated optical-intensity distribution was developed and presented in separate publication.[29]

TABLE I. Simulated PIIES interference pattern performance.

		Lattice constants				
θ_S (deg)	d_{beam} (mm)	a_{sq0} (μm)	Δa_{sq} (%)	a_{hex0} (μm)	Δa_{hex} (%)	A_{SP} (mm^2)
5	4.95	2.952	3.1	2.783	3.1	60.82
10	9.82	1.481	2.9	1.397	2.9	55.42
15	14.53	0.994	2.7	0.937	2.7	50.27
20	19.02	0.752	2.3	0.709	2.3	45.36
25	23.25	0.609	1.9	0.574	1.9	40.72
30	27.19	0.514	1.5	0.485	1.5	19.63

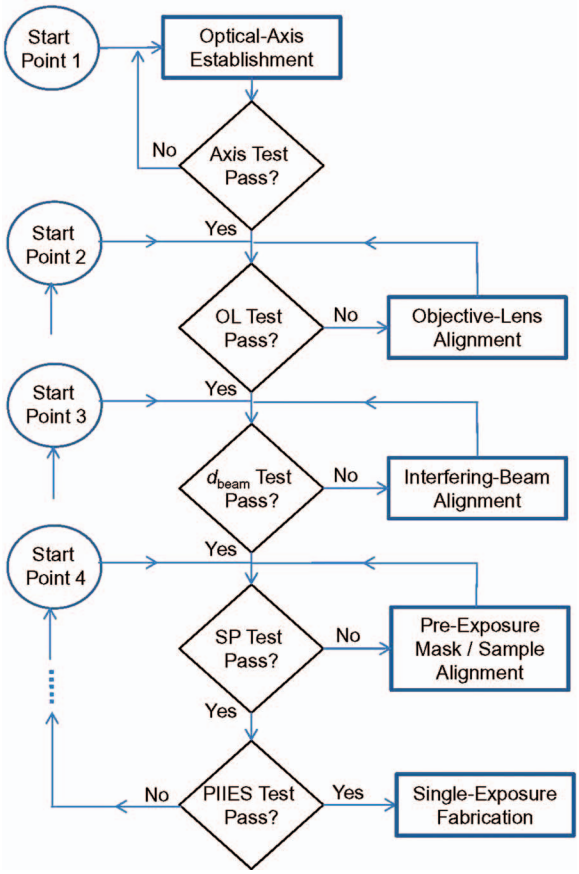

FIG. 4. PIIES alignment flowchart. After all of the alignment tests are successfully passed, the system is ready for a PIIL exposure.

III. EXPERIMENTAL CONFIGURATION

A prototype experimental configuration was constructed to implement the three-beam PIIES configuration depicted in Fig. 1(a). A Spectra-Physics argon-ion UV laser was used as the PIIES source, operating at a single-line wavelength of 363.8 nm with an output power of 75 mW and a beam diameter of 1.7 mm. To ensure a high-contrast interference pattern for a wide range of periodic-lattice symmetries, a combination of half-wave plates and beam-splitter cubes were used to control individual-beam linear polarizations and amplitudes.[19,31] Three large-diameter commercially available broadband antireflection-coated aspheric lens were used for the condenser and first objective lens (Thorlabs, AL100200-B) and the second objective lens (Thorlabs, AL7560-A). The condenser lens was mounted on a two-axis (x and z axes) translational stage. The first objective lens was mounted on a one-axis (z axis) translation stage, and the final objective lens was mounted on a three-axis (x, y, and z axes) translational stage. Mounted small diameter aspheric lenses (Thorlabs, A220TM-A) were used for the three expander lenses, each mounted on compact dovetail three-axis linear-translation platforms. A four-inch chrome pattern mask was positioned using a three-axis translating pattern-mask mount. Similarly, a two-axis (x and z) translating sample mount was used to position the sample for exposure.

Both MBI and projection imaging systems present unique implementation challenges. Specifically, opto-mechanical stability and individual-beam control are paramount in interferometric systems, while precise objective-lens alignment and sample plane positioning are required for successful projection imaging. These implementation challenges are compounded in the PIIES prototype presented here. Accordingly, specific system alignment techniques were developed to ensure proper PIIES functionality. A basic flowchart describing the various steps required to align the system is depicted in Fig. 4. Each alignment execution procedure is described in more detail later in this section. In the alignment presented here, the first requirement is to establish the optical axis of the system. Once the physical axis is established, the subsequent sequential alignment steps may be performed. Of note, the experimental fabrication process described in Sec. IV may require that an alignment execution step be repeated. For this reason, multiple starting points are included in the flowchart.

A. Optical-axis establishment

A rough alignment of all optical components is completed by securing the bases of all components to the table at the approximate locations specified by the ZEMAX optimization described in Sec. II B. Next, an optical system axis is established with a single beam from the UV laser source. This axis beam is adjusted such that it remains parallel to the table, propagating in the (z direction, as depicted in Fig. 5(a). Next, a mask is secured in the mask mount and positioned such that a

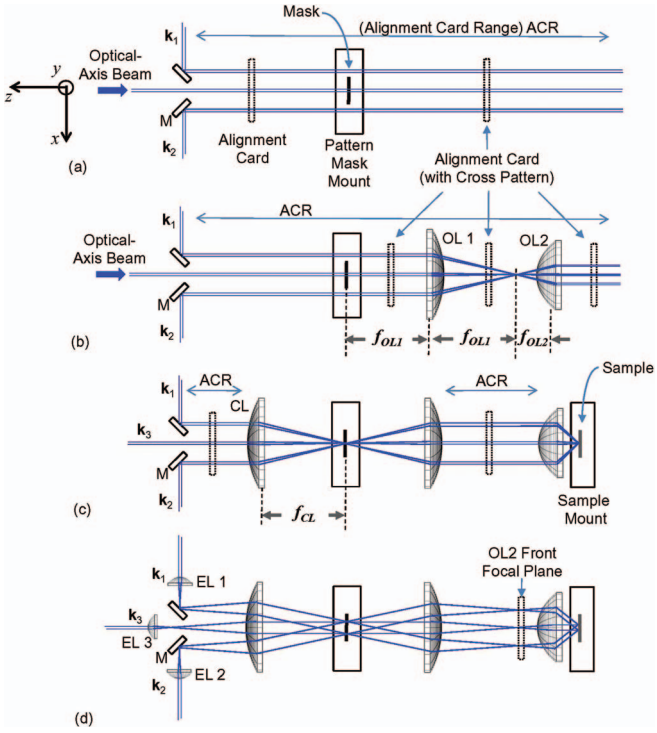

FIG. 5. PIIES alignment and build sequence. (a) The optical axis is established with an alignment card and a diffractive mask element centered on the axis beam. (b) The two objective lenses are centered on the optical axis using the diffraction pattern from the mask element. (c) The condenser lens is positioned and the interfering beams are aligned to the required positions on the alignment card. (d) Expander lenses are added to provide collimated beams at the sample plane and coherent illumination of the pattern mask.

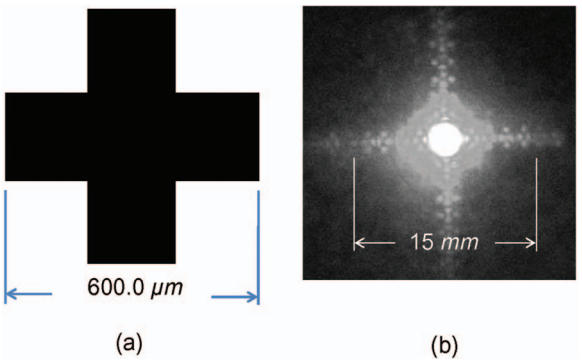

FIG. 6. Diffractive mask feature. (a) A Greek cross on the pattern mask is centered on the axis beam to create a unique diffraction pattern. (b) The resulting crosshair pattern is used to establish the optical axis of the system and align the objective lenses.

single diffractive feature, such as the Greek cross in Fig. 6(a), is positioned in the center of the axis beam. The Greek cross creates a diffraction pattern that resembles a crosshair as depicted in Fig. 6(b) allowing for easy identification of the optical axis of the system. Next, appropriate opto-mechanical guides are established for an alignment card as depicted in Fig. 7 such that the diffraction pattern is centered on the alignment card as it translates along the length of the table (z axis), identified by the alignment card range (ACR) arrow in Fig. 5(a). The alignment card and opto-mechanical guides with the diffractive pattern from the mask that remains centered on the alignment card along the length of the table now define the optical axis of the system (*Axis Test* in Fig. 4).

Before the lenses are added to the configuration, it is prudent to perform an initial alignment of the three interfering beams along the ACR as depicted in Fig. 5(a) ($\mathbf{k}_3$ is not shown for clarity but is parallel to $\mathbf{k}_1$ and $\mathbf{k}_2$ and lies out of the plane of the page and is distinct from the axis beam). This will aid in the final alignment of the interfering beams as discussed in more detail later in this section. To perform the initial interfering-beam alignment, the beam-directing mirrors are adjusted such that the multiple beams are incident on the desired radial beam displacement (d_{beam}) marks on the alignment cards for a square lattice as depicted in Fig. 7(a) or a hexagonal lattice in Fig. 7(b). For example, a square lattice with a lattice constant of $a_{\text{sq}} = 1.0\ \mu\text{m}$ ($\theta_S = 14.9°$) is obtained when the three beams are adjusted such that they intersect the horizontal and vertical radial lines at $d_{\text{beam}} = 14.4$ mm as determined by the ZEMAX optimization described in Sec. II. The initial interfering-beam alignment is complete when the beams remain stationary at the desired beam displacement marks on the alignment card along the length of the ACR.

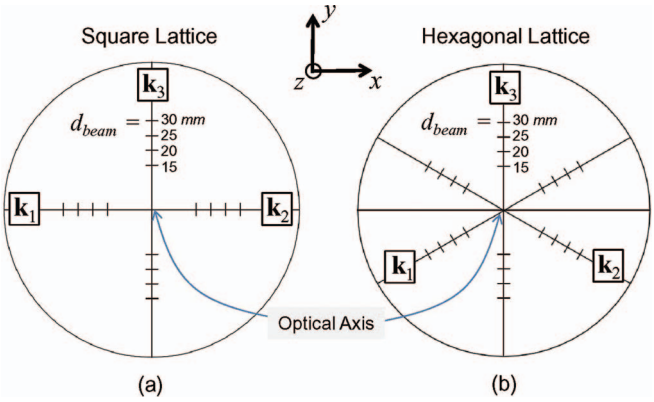

FIG. 7. Alignment cards for (a) a square and (b) a hexagonal lattice.

B. Objective-lens alignment

In a properly aligned objective lens system, the Greek cross diffraction pattern remains centered on the alignment card before and after each objective lens, and all beams enter and exit the objective lens system parallel to the optical axis (*OL Test* in Fig. 4).

After establishing the optical axis, the first objective lens (OL1) is placed after the mask at a distance such that the mask is at the front focal plane of OL1, as depicted in Fig. 5(b). All tilt and decentration are removed from the lens such that it is orthogonal to and centered on the optical axis of the system. When properly aligned, the diffractive pattern of Fig. 6(b) remains centered on the alignment card along the ACR with the cross focused at infinity after the lens.

To complete the objective lens system build, the second objective lens (OL2) is added to the system. Again, all tilt and decentration are removed from OL2 such that it is orthogonal to and centered on the optical axis of the system, and the diffraction pattern remains centered on the alignment card along the ACR after OL2. Next, OL2 is adjusted such that the spacing between the two objective lenses is equal to the sum of the focal lengths of OL1 and OL2 as depicted in Fig. 5(b). In this configuration, the two previously aligned beams on the horizontal axis ($\mathbf{k}_1$ and $\mathbf{k}_2$) enter and exit the objective lens system parallel to the optical axis and in the same relative position on the alignment card. Of course, the beam displacements after the second objective lens will be adjusted according to the ratio of focal lengths of the two objective lenses.

C. Interfering-beam alignment

In a properly aligned PIIES, all three off-axis beams remain centered on the correct radial points on the alignment card, corresponding to the required beam displacement d_{beam}, along the ACR before the CL and between OL1 and OL2 (*SP Test* in Fig. 4).

To ensure that the multiple beams are centered on origin at the mask plane (second optimization requirement in Sec. II B), the CL is added to the system with the mask plane located at the CL back focal plane as depicted in Fig. 5(c). All tilt and decentration are removed from the lens such that it is orthogonal to and centered on the optical axis of the system. To satisfy the positioning requirements, the CL is adjusted such that all three interfering beams are focused to a common on-axis point at the mask plane. In the configuration presented here, all three focused beams will be blocked simultaneously by the on-axis Greek cross when the CL is properly aligned.

To ensure axial propagation of the beams between OL1 and OL2 (third optimization requirement in Sec. II B) and set

the specific value of θ_S at the sample plane (sixth optimization requirement in Sec. II B), OL1 is adjusted along the optical axis such that the three beams are incident on the alignment card at the correct positions along the ACR between OL1 and OL2 as depicted in Fig. 5(c). Of note, the beam positions are now inverted but at the same required radial d_{beam} distances.

Finally, to ensure collimation of the beams at the mask plane (first optimization requirement in Sec. II B) and collimation of the beams at the sample plane (fourth optimization requirement in Sec. II B), each expander lens is added and adjusted such that each beam is incident on the alignment card at the required position for the desired lattice constant and focuses to a point at the front focal plane of OL2 as depicted in Fig. 5(d).

D. Pre-exposure mask/sample alignment

The PIIES is aligned for the first exposure in the experimental process when the sample plane is positioned approximately at the image plane of the objective lens system (*SP Test* in Fig. 4). As discussed earlier in this section, a CCD camera may be used to confirm the basic pattern-integrated imaging properties of the system. This is particularly useful in gaining an appreciation for the effects of adjustments to various components on the pattern-integrated image in real time. However, prior to any experimental fabrication it is important to determine an appropriate initial starting position for the sample mount with the surface of the sample positioned approximately at the in-focus image plane.

As a final step before PIIES exposure, the sample plane mount is positioned such that the multiple beams intersect at a common point centered on the origin at the sample plane (fifth optimization requirement in Sec. II B). In this step, the expander lenses are temporarily removed from the system and the sample mount is placed after OL2, as depicted in Fig. 5(c). Next, an opaque glass slide (with the same dimensions as the sample that will be used in the exposure) is placed in the sample mount. The sample mount is then adjusted along the z axis such that all three beams focus to a point at the front plane of the opaque glass slide. The micrometer position for the sample mount axial translation stage, z_{SP0}, is recorded and will serve as the initial-focused position in the experimental procedures presented in Sec. IV. The expander lenses are placed back into the system and the PIIES is now properly aligned for an experiment.

IV. EXPERIMENTAL PROCEDURES AND RESULTS

A basic lithographic exposure procedure was used to record the PIIES optical-intensity distribution in a thin layer of positive photoresist on a 31.75 mm square UV-grade fused quartz slide. First, each slide was chemically cleaned and layered with 1 μm of Shipley SC1813 positive photoresist using a SCS G3P8 Spin Coater. After a 4 min soft bake, each slide was exposed for 0.7 s. The x axis translation stage for the sample mount allowed for multiple exposures on one prepared slide by adjusted the horizontal position of the slide between exposures. Typically, this procedure allowed for up to eight exposures on one slide. Once the final exposure was complete the slide was developed with a 30 s agitation bath of Microposit MF-319 Developer.

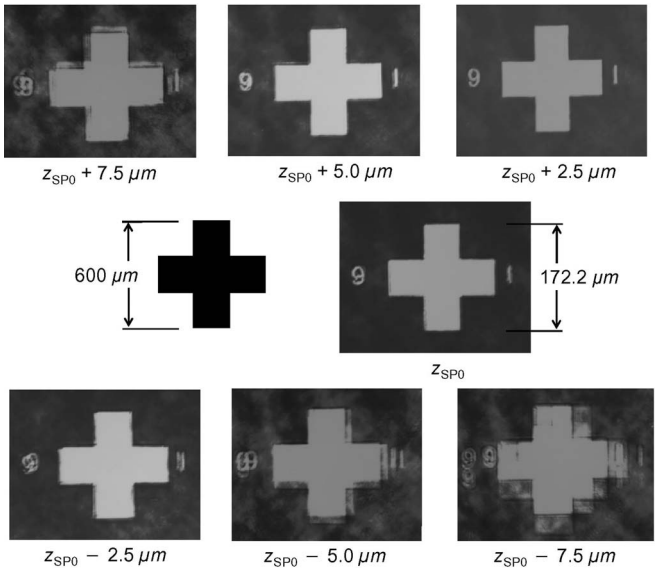

FIG. 8. Experimental focusing of PIIES. CCD image captures using an Olympus NC60 microscope depict fabricated pattern-integrated images of a Greek cross at z_{SP0} + 7.5, z_{SP0} + 5.0, z_{SP0} + 2.5, z_{SP0}, z_{SP0} − 2.5, z_{SP0} − 5.0, and z_{SP0} − 7.5 μm.

A. Pattern-integrated image focusing procedures

To find the precise location of the plane of best focus, two basic experimental procedures were followed. First, a set of initial coarse-focusing exposures was conducted at 2.5 μm intervals centered around the initial-focused position, z_{SP0}, obtained during the pre-exposure alignment. For example, a set of seven exposures would include micrometer positions of z_{SP0} + 7.5, z_{SP0} + 5.0, z_{SP0} + 2.5, z_{SP0}, z_{SP0} − 2.5, z_{SP0} − 5.0, and z_{SP0} − 7.5 μm. The initial coarse-focusing exposures were conducted with a relatively large mask feature on axis, such as the Greek cross in Fig. 6(a). The exposed slide was then developed and evaluated directly using an Olympus NC60 microscope with a maximum of 100× magnification in the reflected-light brightfield observation mode. This procedure allows for relatively simple and efficient experimental focusing without the need for complicated sample processing or scanning electron microscope (SEM) imaging. Figure 8 depicts example CCD image captures of the Greek cross at various axial sample-mount micrometer positions. From this initial set of coarse-focusing exposures, a new coarse-focused micrometer position, z_{SP1}, is established. For example, the series of CCD images in Fig. 8 would establish a course-focused position of approximately $z_{\text{SP1}} = z_{\text{SP0}} + 1.5$ μm.

Next, a set of fine-focusing exposures was conducted at 0.5 μm intervals centered around the course focused position, z_{SP1}. This set of exposures should identify a fine-focused micrometer position, z_{SP2}, for the sample mount. Once this final sample mount position is established, the system is ready for PIIL exposure. In the research presented here, exposures of

the Greek cross were made. In addition, smaller mask features were positioned on axis for pattern-integrated imaging of representative photonic crystal structures. The final exposed slides presented in Sec. IV B were developed and layered with 20 nm of Au/Pd using a Hummer 6 Gold Sputterer and imaged using a Zeiss Ultra60 SEM.

B. Single-exposure fabrication results

Through careful system alignment and experimental focusing procedures, the PIIES pattern-integrated optical-intensity distribution was successfully recorded in a positive photoresist in a single-exposure step for two representative fundamental PC structures, a cavity and a waveguide. Similar results are presented in a separate publication and include comparisons to simulation results.[29] The basic results repeated here demonstrate the fabrication capabilities of our PIIES prototype using the alignment and experimental procedures presented in the current work.

First, a relatively large mask feature consisting of a 600.0 × 600.0 μm Greek cross as depicted in Fig. 9(a) was illuminated with the three off-axis interfering beams and projected to a size of 172.2 × 172.2 μm. The resulting pattern-integrated optical-intensity distribution is depicted in the SEM image of Fig. 9(b). Next, a magnified SEM view of a corner of the projected cross is depicted in Fig. 9(c) corresponding to the solid outlined area in Fig. 9(b). Here, the surrounding square PC lattice is revealed, defined by black circular regions corresponding to the intensity maxima of the periodic pattern (grey areas indicate areas of intensity minima, while the white areas represent the transition between the points of maximum and minimum intensity). A MATLAB (Ref. 36) generated grayscale intensity scale bar is included in Fig. 9(c) to provide an approximation of the relative intensity values recorded in the photoresist. In this first experiment, the cross successfully blocked all three beams, preventing the formation of the periodic interference pattern within the projected cross, while transitioning to a well-defined PC lattice within the distance of one lattice constant, demonstrating PIIL's ability to define abrupt transitions within a lattice, such as a PC cavity.

To demonstrate PIIL's ability to fabricate smaller PC structures, such as a single PC waveguide, a single line segment with mask dimensions of 2.0 × 20.0 μm as illustrated in Fig. 10(a) was illuminated with the three beams and projected to a size of 0.6 × 5.8 μm as depicted in the SEM image of Fig. 10(b). A magnified SEM view of the fabricated line segment is depicted in Fig. 10(c) showing the successful elimination of a single row of PC-lattice points. Small deviations of the experimental opto-mechanical system from the perfectly aligned configuration used in the simulation may account for the qualitative differences between predicted and experimental results. Even with the opto-mechanical deviations present in the PIIES prototype, the experimental results presented in Fig. 10 demonstrate the ability of the PIIL to fabricate, in a single-exposure step, a PC waveguide, a fundamental structure in most PC devices. This represents the first

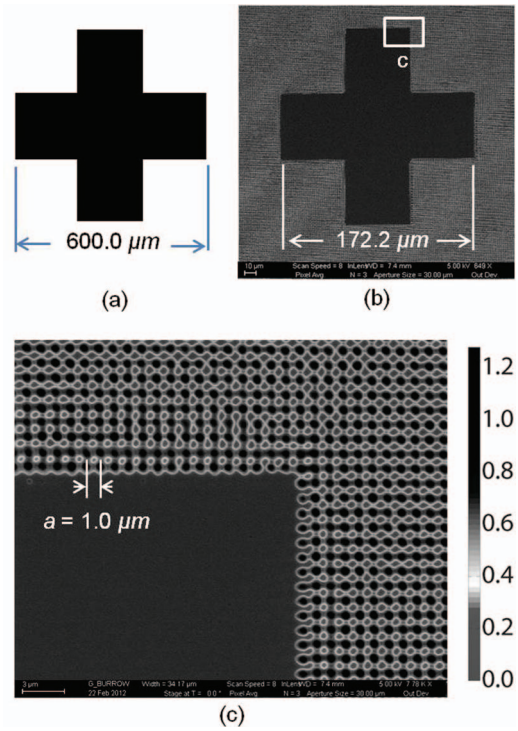

FIG. 9. PIIES single-exposure fabrication results. (a) A pattern-mask feature of a 600.0 × 600.0 μm Greek cross is projected to a size of 172.2 × 172.2 μm. (b) A SEM image depicts the resulting single-exposure PIIES optical-intensity distribution of the projected cross and interference pattern. (c) A magnified SEM view of a corner of the fabricated corss depicts a well-defined corner produced by the projected Greek cross surrounded by the interferomatrically defined square PC lattice with a periodicity of $a = 1.0$ μm.

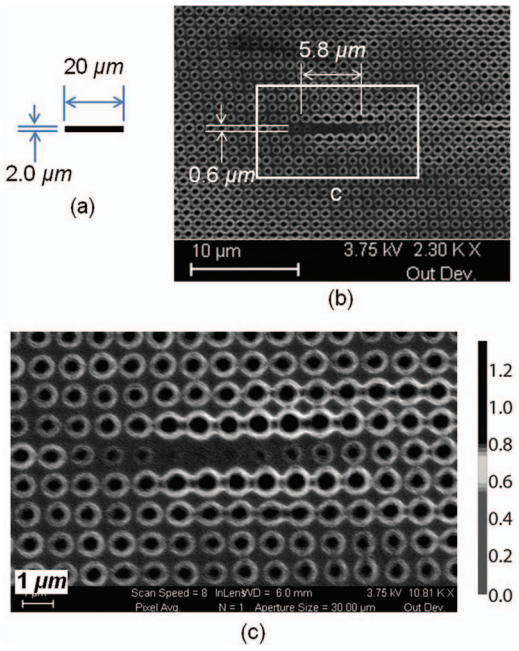

FIG. 10. Demonstration of PIIL single-exposure PC waveguide fabrication. (a) A pattern-mask feature of a 2.0 × 20.0 μm line segment is projected to a size of 0.6 × 5.8 μm. (b) A SEM image depicts the resulting single-exposure PIIES optical-intensity distribution of the projected line segment and square-lattice PC. (c) A magnified SEM view of the line segment depicts the selective elimination of a single row of lattice points in the surrounding periodic lattice, demonstrating the ability of the PIIL to fabricate a PC waveguide, the fundamental element of most PC devices.

single-exposure fabrication of a basic PC waveguide structure via the integration of superposed pattern imaging with IL.

For the PIIES presented here, the total interference area is approximately 4 mm^2. Larger interference areas are possible as expander lens focal lengths are decreased, resulting in larger collimated interfering-beam diameters at the sample plane as discussed in Sec. II C. From SEM images of the center and of the periphery of the interference area, the lattice constants were typically in the range from 1.02 to 1.06 μm. This small variation in lattice constant values is in good agreement with the predicted performance presented in Sec. II. Lattice-vector angles for **a** and **b,** as depicted in Fig. 1(b), varied typically by less than 1°. These results demonstrate excellent uniformity across the entire periodic pattern.

Based on ZEMAX simulations, the present PIIES configuration is capable of sub-500 nm periodicities with still smaller periodic features. In other PIIES experiments, lattice constants near 600 nm were achieved.[27] Of course, for smaller lattice periodicities, the required beam displacement d_{beam} depicted in Fig. 2 increases, placing the interfering beams near the limits of the clear apertures of the objective lenses. As a consequence, less of the diffracted energy from the projected mask features is collected by the objective lenses. In addition, lens aberrations are more pronounced near the aperture limits for off-axis illumination. This, in turn, degrades the quality of the projected mask features. For this reason, the beam displacements were adjusted to be well within the clear aperture limits of the objective lens to assist in focusing the projected mask features for the experimental fabrications presented here. This resulted in a lattice periodicity of 1.0 μm. The initial fabrication results obtained with this relatively simple PIIES prototype and basic experimental procedures demonstrate the fundamental PIIL patterning capability. Future results are expected to be improved with advanced systematic objective lens design (e.g., larger numerical aperture and reduced aberrations), improved opto-mechanical stability and alignment, and advanced lithographic processing techniques.

V. DISCUSSION

The basic design of a PIIES prototype experimental configuration was presented in the current work. Detailed system alignment and experimental procedures were discussed, serving as a foundation for future system design and enhancements. Finally, examples of well-defined PC structures were presented, representing the first ever, to the best of the authors' knowledge, fabrication of these structures via the integration of superposed pattern imaging with IL in a single-exposure step. These results also confirm the potential of PIIL for single-exposure fabrication of a wide range of periodic structures with integrated functional elements. With future research, improved optical system design, and refined processing considerations, PIIL holds the promise of commercially cost-effective wafer-scale fabrication of dense integrated optical circuits. Until now, the application of IL was typically limited to strictly periodic patterns with limited control over space-group symmetries and motif geometries. With the PIIES configuration presented here, a wide variety of sub-wavelength periodic patterns with integrated non-periodic features is now possible in a single-exposure step.

While the current research has focused on the demonstration and fabrication of PC structures, PIIL has the potential to impact an increasingly wide variety of application areas. In fact, IL is already the subject of research and commercial development in the micro- and nanoelectronics industry. Using the PIIL methodology presented here, multiple IL and traditional optical lithography exposures may be combined into a single step. With new circuit layouts, refined fabrication techniques, and enhanced PIIES designs, PIIL may also find significant application in the semiconductor industry, extending the use of optical lithography.

ACKNOWLEDGMENTS

This work was supported in part by Grant No. ECCS 0925119 from the National Science Foundation (NSF).

APPENDIX: ZEMAX SYSTEM OPTIMIZATION

The PIIES configuration developed in Sec. II was modeled with ZEMAX (Ref. 30) using the specifications for commercial large-diameter aspheric UV lenses. A Thorlabs[34] 100 mm diameter, 200 mm focal length aspheric lens (AL100200-B) was selected for both the condenser lens and the first objective lens. A Thorlabs 75 mm diameter, 60 mm focal length

TABLE II. PIIES lens data.

Surface type	No.	Radius (mm)	Thickness (mm)	Semi-diameter (mm)	Note
Even asphere	1	5.97	5.00	5.00	Expander lens—see Table III
Standard	2	−72.47	Variable	5.00	
Coordinate break	3		0.00	0.00	Decenter Y (mm)—variable
Even asphere	4	102.24	19.00	5.00	Condenser lens—see Table III
Standard	5	Infinity	Variable	0.00	
Standard	6	Infinity	Variable	0.00	
Standard	7	Infinity	19.00	50.00	
Even asphere	8	−102.24	Variable	50.00	Objective lens 1—see Table III
Even asphere	9	43.84	35.50	37.50	Objective lens 2—see Table III
Standard	10	Infinity	Variable	37.50	
Standard	11	Infinity	0.00	0.00	

TABLE III. PIIES aspheric lens equation data.

	Aspheric lens equation term						
No.	Conic	2nd order	4th order	6th order	8th order	10th order	12th order
2	0.00		-3.383558×10^{-4}	-1.30539×10^{-5}	1.09825×10^{-6}	-1.374268×10^{-7}	5.49555×10^{-9}
6	−1.317766		8.682×10^{-8}	1.7733×10^{-13}	1.9032×10^{-17}		
10	−1.317766		-8.682×10^{-8}	-1.7733×10^{-13}	-1.9032×10^{-17}		
11	−0.750486	4.713×10^{-3}	1.615609×10^{-6}	3.725877×10^{-10}	9.893012×10^{-14}	1.099179×10^{-17}	

aspheric lens (AL7560-A) was selected for the second objective lens. A mounted Thorlabs 6.48 mm diameter, 11 mm focal length aspheric lens (A220TM-A) was selected for the three expander lenses. Based on the Thorlabs specification sheets for each lens, the optical system lens data used in the ZEMAX simulation is listed in Tables II and III.

The ZEMAX optimization method used to determine the optimal PIIES configuration employs a routine that seeks to find a local minimum for the merit function

$$MF^2 = \sum W_i \, (V_i - T_i)^2 \Big/ \sum W_i, \qquad \text{(A1)}$$

where W is the absolute value of the weight of the operand, V is the current value, T is the target value, and i indicates the operand number.[35] To satisfy the six optimization requirements in Sec. II, the following operands were included in the merit function: (1) RAID (Px = 0, Py = 0) − RAID (Px = 0,±1, Py = ±1,0) = 0 at surface 6, (2) REAX and REAY = 0 at surface 6, (3) RAID (Px = 0, Py = 0) = 0 at surface 9, (4) RAID (Px = 0, Py = 0) − RAID (Px = 0,±1, Py = ±1,0) = 0 at surface 11, (5) REAX and REAY = 0 at surface 11, and (6) RAID (Px = 0, Py = 0) = target incidence angle at surface 11. Here, RAID is the ray angle of incidence with respect to the surface normal, REAX and REAY are the ray x- and y-coordinate positions at the specified surface, and Px and Py are the normalized pupil coordinates.

[1] G. M. Burrow and T. K. Gaylord, Micromachines **2**, 221 (2011).
[2] D. Xia, Z. Ku, S. C. Lee, and S. R. J. Brueck, Adv. Mater. **23**, 147 (2011).
[3] V. Berger, O. Gauthier-Lafaye, and E. Costard, Electron. Lett. **33**, 425 (1997).
[4] M. Campbell, D. N. Sharp, M. T. Harrison, R. G. Denning, and A. J. Turberfield, Nature (London) **404**, 53 (2000).
[5] R. C. Rumpf and E. G. Johnson, J. Opt. Soc. Am. A **21**, 1703 (2004).
[6] E. L. Hedberg-Dirk and U. A. Martinez, J. Nanomater. **2010**, 1767501 (2010).
[7] J.-H. Jang, D. Dendukuri, H. T. Alan, E. L. Thomas, and P. S. Doyle, Angew. Chem., Int. Ed. **46**, 9027 (2007).
[8] F. A. Zoller, C. Padeste, Y. Ekinci, H. H. Solak, and A. Engel, Microelectron. Eng. **85**, 1370 (2008).
[9] E. Schonbrun, R. Piestun, P. Jordan, J. Cooper, K. D. Wulff, J. Courtial, and M. Padgett, Opt. Express **13**, 3777 (2005).
[10] A. E. Chiou, W. Wang, G. J. Sonek, J. Hong, and M. W. Berns, Opt. Commun. **133**, 7 (1997).
[11] P. Jakl, T. Cizmar, M. Sery, and P. Zemanek, Appl. Phys. Lett. **92**, 11101 (2008).
[12] N. Feth, C. Enkrich, M. Wegener, and S. Linden, Opt. Express **15**, 501 (2007).
[13] Y. Yang, Q. Z. Li and G. P. Wang, Opt. Express **16**, 11275 (2008).
[14] D. Sawaki and J. Amako, Proc. SPIE **6459**, F1 (2007).
[15] J. P. Spallas, A. M. Hawryluk, and D. R. Kania, J. Vac. Sci. Technol. B **13**, 1973 (1995).
[16] C. H. Liu, M. H. Hong, H. W. Cheung, F. Zhang, Z. Q. Huang, L. S. Tan, and T. S. A. Hor, Opt. Express **16**, 10701 (2008).
[17] M. Duarte, A. Lasagni, R. Giovanelli, J. Narciso, E. Louis, and F. Mucklich, Adv. Eng. Mater. **10**, 554 (2008).
[18] R. Murillo, H. A. van Wolferen, L. Abelmann, and J. C. Lodder, Microelectron. Eng. **78–79**, 260 (2005).
[19] G. M. Burrow and T. K. Gaylord, in *Frontiers in Optics*, Rochester, New York, 2010 (Optical Society of America, 2010), paper FWS3.
[20] L. Z. Cai, X. L. Yang, and Y. R. Wang, Opt. Lett. **27**, 900 (2002).
[21] A. I. Petsas, A. B. Coates, and G. Grynberg, Phys. Rev. A **50**, 5173 (1994).
[22] L. J. Wu, Y. C. Zhong, K. S. Wong, G. P. Wang, and L. Yuan, Appl. Phys. Lett. **88**, 091115 (2006).
[23] L. Z. Cai, X. L. Yang, and Y. R. Wang, J. Mod. Opt. **49**, 1663 (2002).
[24] J. L. Stay and T. K. Gaylord, Appl. Opt. **48**, 4801 (2009).
[25] L. Z. Cai, X. L. Yang and Y. R. Wang, Opt. Lett. **26**, 1858 (2001).
[26] J. L. Stay and T. K. Gaylord, Appl. Opt. **47**, 3221 (2008).
[27] G. M. Burrow and T. K. Gaylord, in *Frontiers in Optics*, San Jose, California, 2011 (Optical Society of America, 2011), paper FWZ2.
[28] G. M. Burrow and T. K. Gaylord, U.S. patent 2012/0081687 (30 September 2010).
[29] G. M. Burrow, M. C. R. Leibovici, and T. K. Gaylord, Appl. Opt. **51**, 4028 (2012).
[30] Zemax Optical Design Program User's Guide (Focus Software, Inc., 2003).
[31] J. L. Stay, G. M. Burrow, and T. K. Gaylord, Rev. Sci. Instrum. **82**, 231151 (2011).
[32] S. Boscolo, M. Midrio and C. G. Someda, IEEE J. Quantum Electron. **38**, 47 (2002).
[33] B. W. Smith, in *Microlithography: Science and Technology*, edited by K. Suzuki and and B. W. Smith (CRC, Boca Raton, 2007).
[34] Thorlabs Ltd., Newton, New Jersey.
[35] Zemax Optical Design Program User's Guide, Focus Software, Inc., Tucson, Arizona, 2003.
[36] The Mathworks Inc., Natick, Massachusetts.